Hindawi Publishing Corporation
International Journal of Chemical Engineering
Volume 2016, Article ID 4596251, 14 pages
http://dx.doi.org/10.1155/2016/4596251

Research Article

Parametric Analysis of a High Temperature PEM Fuel Cell Based Microcogeneration System

Myalelo Nomnqa, Daniel Ikhu-Omoregbe, and Ademola Rabiu

Department of Chemical Engineering, Faculty of Engineering, Cape Peninsula University of Technology, Keizersgracht and Tennant Street, Zonnebloem, P.O. Box 652, Cape Town 8000, South Africa

Correspondence should be addressed to Myalelo Nomnqa; myalelo.nomnqa@outlook.com

Received 23 March 2016; Accepted 22 May 2016

Academic Editor: Deepak Kunzru

This study focuses on performance analysis of a 1 kW_e microcogeneration system based on a high temperature proton exchange membrane (HT-PEM) fuel cell by means of parametric investigation. A mathematical model for a system consisting of a fuel processor (steam reforming reactor and water-gas shift reactor), a HT-PEM fuel cell stack, and the balance-of-plant components was developed. Firstly, the fuel processor performance at different fuel ratios and equivalence ratio was examined. It is shown that high fuel ratios of 0.9–0.95 and equivalence ratios of less than 0.56 are suitable for acceptable carbon monoxide content in the synthetic gas produced. Secondly, a parametric study of the system performance at different fuel and equivalence ratios using key system operating parameters was conducted. Steam-to-carbon ratio, stack operating temperature, and anode stoichiometry were varied to observe the changes in the microcogeneration system. The analysis shows that the system can reach electrical and cogeneration efficiencies of 30% and 84%, respectively.

1. Introduction

Because of the inefficiency and pollution associated with centralized power generation, there has been growing interest in shifting to distributed (decentralized) power generation systems. Cogeneration (or Combined Heat and Power (CHP)) is seen to have the potential to primary energy savings and greenhouse gas emissions reduction when compared with large power stations [1, 2]. Cogeneration is the combined production of electrical and thermal energy from a single primary energy source. In residential applications, cogeneration provides electricity and heat (for hot water and space heating) for the household. Fuel cells, specifically the polymer electrolyte membrane (PEM) fuel cell and the solid oxide fuel cell (SOFC), are considered as an alternative to combustion based technologies utilized to meet heating requirements. This is because they exhibit high efficiencies, low emissions and noise levels, modularity, and a low heat-to-power ratio [3]. The low temperature PEM (LT-PEM) fuel cells are the most developed and widely studied type of PEM fuel cell, operating at relatively low temperatures (<80°C) and have Nafion based membrane. Microcogeneration systems based on LT-PEM fuel cell have been widely demonstrated and have enjoyed some commercialization success [4]; there are however disadvantages associated with this stack technology. For instance, the proton conduction mechanism of Nafion membrane requires water management systems to prevent MEA flooding/drying. The low operating temperature makes the LT-PEM fuel cell be susceptible to carbon monoxide poisoning and thus requires 99.99% hydrogen-rich gas.

The development of a high temperature PEM (HT-PEM) fuel cell which operates at higher temperature (120°C–200°C) has overcome these issues. Because the proton conduction mechanism in the polybenzimidazole- (PBI-) based HT-PEM fuel cell is dependent on the phosphoric acid content and not on the membrane water content [5, 6], the need for complex water management systems is eliminated, thus simplifying the system design. The high temperature operation improves the PEM fuel cell performance and has operational advantages, such as tolerance to carbon monoxide (CO) levels [7–10]. The HT-PEM fuel cell has a tolerance of CO of up to 3% in hydrogen at 0.8 A cm^{-2} and 200°C as reported by Li

et al. [10]. The improved tolerance to CO allows use of a synthetic gas from various fuel sources without the need for complex CO clean-up systems [11–15]. Gardemann et al. [11] demonstrated a compact ethanol fuel processor for small scale system (200 W–500 W) [11]. Maximini et al. [12] reported on the development of a steam reforming based fuel processor for diesel operation. Samsun et al. [13] explored a start-up strategy based on utilization of electrical heaters at different locations in the fuel processor to heat process air of diesel and kerosene fuel processor via modeling and experiments. They reported an improved start-up time of the fuel processor from 22 min to 9.5 min when the strategy is applied. Authayanun et al. [14] analyzed the integration of a glycerol fuel processor and a HT-PEM. They considered the effects of steam-to-carbon ratio (S/C) and reforming temperature on the reformate gas composition. Similarly, Perna et al. [15] conducted a sensitivity analysis of a LPG reformer coupled with a membrane shift reactor for a 5 kW system with results showing the reforming pressure as a critical parameter for improved fuel processor performance.

Recently there has been increased interest in studying cogeneration systems based on HT-PEM fuel cell. Authayanun et al. [16] conducted a comparison study of a 3 kW_e cogeneration system, based on HT-PEM and LT-PEM fed with pure hydrogen, and using a reformate gas from a glycerol reformer. The LT-PEM system demonstrated better performance for pure hydrogen operation, while the HT-PEM system exhibited better performance for reformate operation at full load (4000 A m^{-2}). Similar results were shown by Jannelli et al. [17] when they compared three cogeneration systems operating at 60°C, 160°C, and 180°C, based on fuel stacks with different membranes. Their results indicated that the HT-PEM systems had electrical and cogeneration efficiencies of 40% and 78%, respectively. Because fuel cell systems do not always operate at design points, as when there is less demand for electrical energy, some authors have studied off-design performance. Arsalis et al. [18] and Zuliani and Taccani [19] investigated partial load performance of a 1 kW_e HT-PEM cogeneration system, with similar results showing that the efficiency increased at partial loads. Both investigations showed that the system balance-of-plant (BoP) components do not have a significant effect on the system performance when the load is reduced. The work done by Najafi et al. [20] showed that the electrical efficiency can be increased from 21.18% to 29.21% and the primary saving index from 6.07% to 17.50% when a LT-PEMFC stack is replaced with an HT-PEM stack in an existing 30 kW_e cogeneration system.

Other researchers have optimized the system performance [21–23]. Rabiu et al. [21] reported on application of heat integration technique to optimize the heat exchanger network of a 2 kW system. Arsalis et al. [22] investigated optimization using two techniques: pinch analysis for maximization of electrical efficiency and mixed integer nonlinear programming for minimization of heat exchanger network (HEN) annual costs. The authors showed that the combination of these two techniques could lead to a lower HEN annual cost of US$8,147/year without affecting electrical efficiency. Arsalis et al. [23] have optimized a heat-pump assisted cogeneration system by considering thermophysical parameters at different loads. Najafi et al. [24] explore the use of operating strategies to mitigate the decay of electrical and thermal power output in the first 15,000 hours of a 30 kW plant. According to their recovery strategy, 422.6 MWh of electricity is generated as compared to the 381.3 MWh generated at normal operation during the system lifetime.

The objective of this study was to establish the effects of fuel processor operating parameters on performance parameters such as component yields from fuel processor, system power outputs, and their related efficiencies. Future studies will incorporate these findings in optimization studies exploring the effect of the cogeneration system operating parameters.

2. Modeling of the Cogeneration System

A schematic representation of the natural gas-fuelled system consisting of two subsystems, the HT-PEM fuel cell and the fuel processing subsystem, is shown in Figure 1. It is assumed that natural gas contains only methane (CH_4).

2.1. Methane Steam Reformer (MSR). The model presented can apply any kinetic model appropriate for the type of catalyst used. In this work, the intrinsic kinetic expressions reported by Xu and Froment [26] for nickel-alumina catalysts that have been widely used in literature are adopted. The reaction kinetics are based on the Langmuir-Hinshelwood reaction mechanism, consisting of the steam reforming reaction and the water-gas shift (WGS) reaction. Two global reaction schemes are considered and are expressed as follows:

$$\mathrm{CH_4 + H_2O \longrightarrow CO + 3H_2} \qquad \Delta H_{298} = 206.1\ \mathrm{kJ\ mol^{-1}}\ \ \text{(MSR)} \tag{1}$$

$$\mathrm{CO + H_2O \longrightarrow CO_2 + H_2} \qquad \Delta H_{298} = -41.2\ \mathrm{kJ\ mol^{-1}}\ \ \text{(WGS)} \tag{2}$$

Their respective rate equations are as follows:

For methane steam reforming,

$$r_1 = \frac{\left(k_1/p_{\mathrm{H_2}}^{2.5}\right)\left[p_{\mathrm{CH_4}}p_{\mathrm{H_2O}} - p_{\mathrm{H_2}}^3 p_{\mathrm{CO}}/K_{\mathrm{eq_1}}\right]}{(\mathrm{DEN})^2}. \tag{3}$$

For water-gas-shift,

$$r_2 = \frac{\left(k_2/P_{\mathrm{H_2}}\right)\left[p_{\mathrm{CO}}p_{\mathrm{H_2O}} - p_{\mathrm{H_2}}p_{\mathrm{CO_2}}/K_{\mathrm{eq_2}}\right]}{(\mathrm{DEN})^2}$$

$$\mathrm{DEN} = 1 + K_{\mathrm{CO}}P_{\mathrm{CO}} + K_{\mathrm{H_2}}P_{\mathrm{H_2}} + K_{\mathrm{CH_4}}P_{\mathrm{CH_4}} + K_{\mathrm{H_2O}}\frac{P_{\mathrm{H_2O}}}{P_{\mathrm{H_2}}}. \tag{4}$$

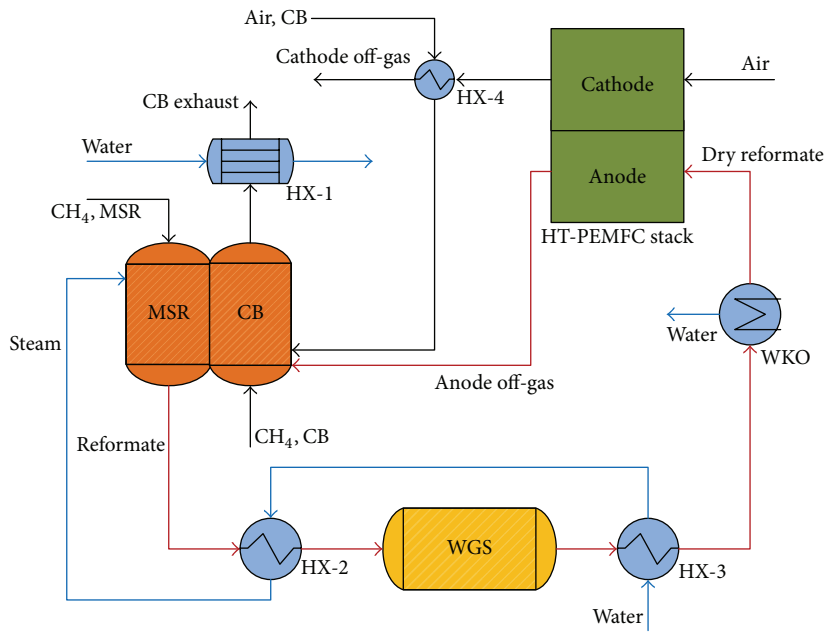

Figure 1: Schematic representation of the HT-PEM fuel cell cogeneration system.

The rate constants and adsorption constants are determined by the Arrhenius and Van't Hoff relations:

$$k_i = A(k_i)\exp\left(-\frac{E_{a,i}}{RT}\right)$$
$$K_j = A(K_j)\exp\left(-\frac{\Delta H_j}{RT}\right) \quad (5)$$
$$(i = 1,2)\ \ (j = H_2, H_2O, CO, CO_2, CH_4).$$

2.2. Water-Gas Shift (WGS). The reformate gases leaving the steam reformer are a mixture of mainly hydrogen (H_2), carbon dioxide (CO_2), water vapor (H_2O), carbon monoxide (CO), and small traces of methane (CH_4). The platinum catalyst used in the fuel cell stack is prone to CO poisoning in the temperature range at which it operates. Thus, to reduce the CO content in the reformate gas, the gas is fed to a shift reactor where the CO reacts with H_2O to produce more H_2. In the WGS reactor the CO content should be reduced to an acceptable level (for the fuel cell stack) of less than 2%. The kinetic model of the WGS reactor is described in detail in Kim et al. [27], and global reaction considered is expressed as follows:

$$CO + H_2O \longrightarrow CO_2 + H_2 \quad \Delta H_{298} = -41.2\,\text{kJ mol}^{-1} \quad (6)$$

$$r_4 = k_0 \exp\left(-\frac{E_a}{RT}\right) p_{CO} p_{H_2}\left(1 - \frac{p_{H_2} p_{CO_2}}{p_{CO} p_{H_2O} K_{eq}}\right) \quad (7)$$

$$K_{eq} = 9.543 \times 10^{-3} \exp\left(\frac{39876}{RT}\right). \quad (8)$$

2.3. Catalytic Combustor. The steam reforming reaction is highly endothermic and needs to be supplied with heat for it to proceed. The anode off-gas is fed to the catalytic combustor, where the unreacted H_2, CH_4, and CO are burned with air to supply the required heat to the steam reformer. Additional CH_4 is also supplied to the combustor because the anode off-gas is not sufficient to maintain the required temperature in the steam reformer. The reactions occurring in the combustor are

$$CH_4 + 2O_2 \longrightarrow 2H_2O$$
$$\Delta H_{298} = -802\,\text{kJ mol}^{-1}\ \text{(Methane combustion)} \quad (9)$$

$$H_2 + 0.5O_2 \longrightarrow H_2O$$
$$\Delta H_{298} = -242\,\text{kJ mol}^{-1}\ \text{(Hydrogen combustion)} \quad (10)$$

$$CO + 0.5O_2 \longrightarrow CO_2$$
$$\Delta H_{298} = -283\,\text{kJ mol}^{-1}\ \text{(Carbon monoxide combustion)} \quad (11)$$

The reaction kinetics of hydrogen (Schefer [28]) methane (Song et al. [29]) and carbon monoxide (Cant et al. [30]) combustion on a platinum catalyst are used.

For methane combustion,

$$r_5 = 1.3 \times 10^{11} \exp\left(-\frac{134{,}700}{RT}\right) y_{CH_4} \sqrt{y_{O_2}}. \quad (12)$$

For hydrogen combustion,

$$r_6 = 1.4 \times 10^{3} \exp\left(-\frac{14979}{RT}\right) c_{H_2}. \quad (13)$$

For carbon monoxide combustion,

$$r_7 = 2.25 \times 10^{5} \exp\left(-\frac{28850}{RT}\right) \frac{p_{CO}}{\left(p_{O_2}\right)^{0.5}}. \quad (14)$$

2.4. HT-PEM Fuel Cell Stack. The fuel cell stack model was developed using a modular approach in which each component (flow channel, gas diffusion layer, and catalyst layer) was

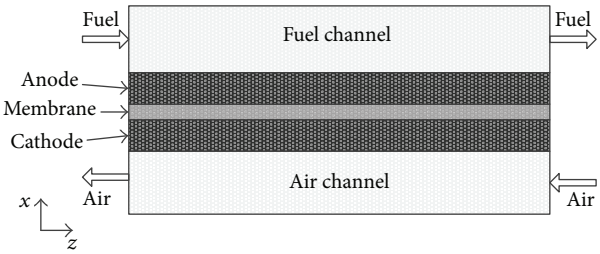

Figure 2: Modeling domain of the HT-PEM fuel cell.

individually modeled and the connectivity equations at the boundaries are used to connect the adjacent layers. Figure 2 shows the schematic of the modeling domain considered in the fuel cell model.

Basic Assumptions

(1) All chemical components of working fluid are considered as ideal incompressible gases, and fully developed laminar flow is considered.

(2) Single phase operation.

(3) Isothermal operation.

(4) No reactant crossover in the electrolyte.

(5) The concentration polarization loss is neglected.

(6) Steady state operation is assumed.

(7) Heat loss to surroundings is negligible.

2.4.1. Gas Channel Subdomain. In the gas channels the consumption of hydrogen and oxygen (O_2) due to electrochemical reactions occurs and water vapor is produced. The conservation of the mass in the presence of electrochemical reactions leads to a set of ordinary differential equations for the rate of change of molar concentrations with respect to axial position within the flow channel. The conservation of mass is solved along the axial coordinate (Z) for the anode and cathode as follows:

$$c_{t,k} u_k \frac{\partial y_{i,k}}{\partial z} = S_i \quad (k = a, c), \tag{15}$$

where c_t is the total gas concentration in the channel, u is the gas velocity, and y_i represents the species molar fractions. The source term S_i represents the species reaction. The source terms of species taking part in the reactions (H_2, O_2, and H_2O) are calculated as

$$\begin{aligned} S_{H_2} &= j\frac{M_{H_2}}{2F} \\ S_{O_2} &= j\frac{M_{O_2}}{4F} \\ S_{H_2O} &= -j\frac{M_{H_2O}}{2F}, \end{aligned} \tag{16}$$

where j represents the current density and M_i the molecular mass of each species. The mass conservation equations are complemented with the associated boundary. The boundary conditions dictate that the molar concentrations of each species at the channel inlet are equal to those of the respective feed stream. A first-order finite difference method (BFDM) with 20 discrete points was used to solve the governing equations in the flow channel.

2.4.2. MEA Subdomain. In MEA five components are included in the model: the anode and cathode gas diffusion layers, the anode and cathode electrodes, and the membrane. Only mass transport due to diffusion is considered in the MEA direction (X). Mass transport in the gas diffusion layer is considered to be 1D along the diffusion flux direction. The Stefan-Maxwell equation is to describe the mass transfer in the GDL:

$$\frac{\partial y_{i,k}}{\partial X} = \sum \frac{y_i N_j - y_j N_i}{c_{t,k} D_{ij}^{\text{eff}}}, \tag{17}$$

where D_{ij}^{eff} is the effective binary diffusion coefficient between species i and j and N_i represents the molar flux of species i. The correlation proposed by Jiao et al. [31] was used to determine the binary diffusion coefficients (18), which were subsequently corrected using Bruggeman's correlation to account for the tortuosity and porosity of porous media (19). A second-order centre finite difference method with 5 discrete points is employed to solve the governing equation in the GDL:

$$D_{ij}\big|_{T,p} = D_{ij}\big|_{T_{\text{ref}},p_{\text{ref}}} \left(\frac{T}{T_{\text{ref}}}\right)^{1.5} \left(\frac{p_{\text{ref}}}{p}\right) \tag{18}$$

$$D_{ij}^{\text{eff}} = \varepsilon^{1.5} D_{ij}. \tag{19}$$

2.4.3. Electrochemical Model. The electrochemical reactions in the HT-PEMFC occur in the thin catalyst zones which are close to the electrode and membrane. In this work it is assumed that electrochemical reactions only occur at the GDL/CL interface, and as such the catalyst layers are modeled as interfaces. This simplification has been widely used in cell-level and system-level analysis. The concentrations of the reacting species (H_2 and O_2) at the catalyst interface are determined using Fick's law of diffusion [32]:

$$\frac{N_i}{S_{\text{Pt},k}} = \frac{-D_i^{H_3PO_4}\left(C_i^{\text{Pt}} - C_i^{\text{eq}}\right)}{\delta_i}. \tag{20}$$

C_i^{Pt} represents the species concentration on the catalyst surface, C_i^{eq} is the equilibrium concentration in the acid thin film at the studied temperature, and δ_i is the film thickness. The concentrations of the species dissolving at the thin film boundary ($C_{i,\text{dissolved}}$) are calculated from their solubility [32]:

$$C_i^{\text{Pt}} = C_{i,\text{dissolved}} y_i P_k, \tag{21}$$

where y_i is the species mole fraction at the electrode/electrolyte interface. The correlations employed by Cheddie and Munroe [33] are used to calculate the solubility and diffusivity of O_2 in phosphoric acid, whereas the diffusivity and solubility of H_2 are assumed to be two times and four times those of O_2, respectively. The activation over voltage due to electrochemical reactions is calculated using the

Butler-Volmer equation for the Oxygen Reduction Reaction and Hydrogen Oxidation Reaction:

$$j_c = i_{o,c}\left[\exp\left(\frac{-\alpha_{\mathrm{Rd},c}nF}{RT}\eta_c\right) - \exp\left(\frac{-\alpha_{\mathrm{Ox},c}nF}{RT}\eta_c\right)\right]$$
$$j_a = i_{o,a}\left[\exp\left(\frac{-\alpha_{\mathrm{Rd},an}nF}{RT}\eta_a\right) - \exp\left(\frac{-\alpha_{\mathrm{Ox},an}nF}{RT}\eta_a\right)\right], \quad (22)$$

where the exchange current density is approximated by

$$i_{o,c} = i_o^{\mathrm{ref}} a_c \left(\frac{C_{\mathrm{O}_2}}{C_{\mathrm{O}_2}^{\mathrm{ref}}}\right)^{\gamma} \exp\left[-7900\left(1 - \frac{T}{T_{\mathrm{ref}}}\right)\right]$$
$$i_{o,a} = i_a^{\mathrm{ref}} a_a \left(\frac{C_{\mathrm{H}_2}}{C_{\mathrm{H}_2}^{\mathrm{ref}}}\right)^{\gamma} \exp\left[-1400\left(1 - \frac{T}{T_{\mathrm{ref}}}\right)\right]. \quad (23)$$

Because of a reformate gas operation, the effect of CO poisoning on the anode catalyst layer is accounted for using a modified the current density (j_a^{CO}) [34]:

$$j_o^{\mathrm{CO}} = j_{o,a}\left(1 - \theta_{\mathrm{CO}}\right)^2, \quad (24)$$

where the temperature dependence of the surface coverage of the reaction site by CO (θ_{CO}) is obtained by correlation employed by Dhar et al. [35]:

$$\theta_{\mathrm{CO}} = 19.9\exp\left(-7.69E - 3T\right) - 0.085\ln\left[\frac{\mathrm{CO}}{\mathrm{H}_2}\right]. \quad (25)$$

The ohmic loss follows Ohm's law and is caused by a resistance of ions in the electrolyte through membrane. The proton conductivity (κ) as a function of temperature and acid doping level (W) follows the Arrhenius law as obtained from Cheddie and Munroe [33]:

$$\kappa = \frac{100}{T}\exp\left[8.0129 - \left(\frac{2605.6 - 70.1W}{T}\right)\right]. \quad (26)$$

The total cell voltage (U_{cell}) is given by

$$U_{\mathrm{cell}} = E_{\mathrm{ocv}} - \eta_{\mathrm{act}} - \eta_{\mathrm{ohm}}, \quad (27)$$

where the thermodynamic equilibrium potential (E_{ocv}) is determined using the Nernst equation:

$$E_{\mathrm{ocv}} = 1.1669 - 0.24\times10^{-3}\left(T - 373.15\right). \quad (28)$$

2.5. Heat Exchangers. The thermal analysis of the heat exchangers is based on the number of transfer units (NTU) method based on the concept of heat exchanger effectiveness (ε). The effectiveness of a heat exchanger is the ratio of the actual heat transfer rate to the thermodynamically limited maximum possible heat transfer rate if an infinite heat transfer surface area was available. For a cross-flow compact heat exchanger with both fluids unmixed, the ε-NTU function is

$$\varepsilon = 1 - \exp\left\{\left(\frac{1}{C_r}\right)\mathrm{NTU}^{0.22}\left[\exp\left(-C_r\mathrm{NTU}^{0.78}\right)\right] - 1\right\}. \quad (29)$$

2.6. System Performance Parameters. The objective functions that are used in the analysis of the system performance are the fuel processor efficiency (η_{FP}), fuel consumption (γ_{CH_4}), electrical efficiency (η_{el}), and cogeneration efficiency (η_{cogen}). The fuel processor efficiency is defined as the ratio of hydrogen produced in the fuel processor and the amount of chemicals available in the input gas (methane) entering the system:

$$\eta_{\mathrm{FP}} = \frac{\left(\dot{m}_{\mathrm{H}_2}\right)_{\mathrm{anode}}\mathrm{LHV}_{\mathrm{H}_2}}{\left(\dot{m}_{\mathrm{CH}_4,\mathrm{in}}\right)_{\mathrm{sys}}\mathrm{LHV}_{\mathrm{CH}_4}}, \quad (30)$$

where $(\dot{m}_{H_2})_{\mathrm{anode}}$ is the mass flow rate of hydrogen at the anode inlet and $(\dot{m}_{\mathrm{CH}_4,\mathrm{in}})_{\mathrm{sys}}$ is the total mass flow rate of methane which is consumed. Fuel conversion/consumption rate is one of the most widely used parameters evaluating fuel processor performance defined as

$$\gamma_{\mathrm{CH}_4} = \left(1 - \frac{\dot{m}_{\mathrm{CH}_4,\mathrm{MSR\ outlet}}}{\dot{m}_{\mathrm{CH}_4,\mathrm{MSR\ inlet}}}\right)\times 100, \quad (31)$$

where $\dot{m}_{\mathrm{CH}_4,\mathrm{MSR\ outlet}}$ is the methane flow rate at the MSR outlet and $\dot{m}_{\mathrm{CH}_4,\mathrm{MSR\ inlet}}$ is methane flow rate at the MSR inlet. The electrical efficiency is defined as the ratio of the electrical power output from the fuel cell stack divided by the chemical energy of the hydrogen from the fuel processor:

$$\eta_{\mathrm{el}} = \frac{P_{\mathrm{el}}}{\left(\dot{m}_{\mathrm{CH}_4,\mathrm{in}}\mathrm{LHV}_{\mathrm{CH}_4}\right)_{\mathrm{system\ inlet}}}, \quad (32)$$

where P_{el} represents the electrical power produced in the fuel cell stack. The system cogeneration efficiency is defined as the sum of the thermal and electrical power divided by the amount of methane which is consumed:

$$\eta_{\mathrm{cogen}} = \frac{P_{\mathrm{el}} + P_{\mathrm{th}}}{\left(\dot{m}_{\mathrm{CH}_4,\mathrm{in}}\mathrm{LHV}_{\mathrm{CH}_4}\right)_{\mathrm{system\ inlet}}}, \quad (33)$$

where P_{th} is the thermal energy recoverable from the cogeneration heat exchanger. The system model was implemented in a commercial application, gPROMS Model Builder version 3.6.0 from PSE Ltd. [36]. The computation station consists of a 64-bit Windows platform, 8 GB RAM, and an Intel(R) Core™ i5 3.20 GHz processor. The gPROMS DASolver is used to solve numerical functions during simulation.

3. Model Validation

The fuel cell characteristics obtained from the model and experimental results from Bujlo et al. [37] at different operating conditions are compared in Figure 3. The model is calibrated using the gPROMS parameter estimation module where the fuel cell electrochemical parameters (Table 1) are estimated to predict the performance of the model to that of the experiment. As can be noted in Figure 3, there is an acceptable agreement between the model and the experimental results, which verifies the validity of the model. To verify the validity of the fuel processor model, the simulation results were compared with results from the literature. Two sets of data were selected for this purpose, experimental data by Di Bona et al. [38] and numerical data by Jung et al. [39].

Table 1: Values of parameters used in HT-PEMFC model.

Parameter	Value
GDL porosity	0.6
Membrane thickness (m)	4×10^{-5}
Anode film thickness (m)	2.5×10^{-9}
Cathode film thickness (m)	1.48×10^{-9}
Anode reference exchange current density (A/m^2)	1440
Cathode reference exchange current density (A/m^2)	0.0004
Anode catalyst surface area (m^2/g)	64
Cathode catalyst surface area (m^2/g)	32.25
Anode catalyst loading (mg/cm^2)	0.2
Cathode catalyst loading (mg/cm^2)	0.4
Transfer coefficient at anode	0.5
Transfer coefficient at cathode	0.5
Anode reference concentration (mol/cm^3)	0.0002
Cathode reference concentration (mol/cm^3)	0.0004
Anode activation energy (kJ/mol)	16000
Cathode activation energy (kJ/mol)	54066
Anode reference cell temperature (K)	433.15
Cathode reference cell temperature (K)	373.15
Reaction order	1

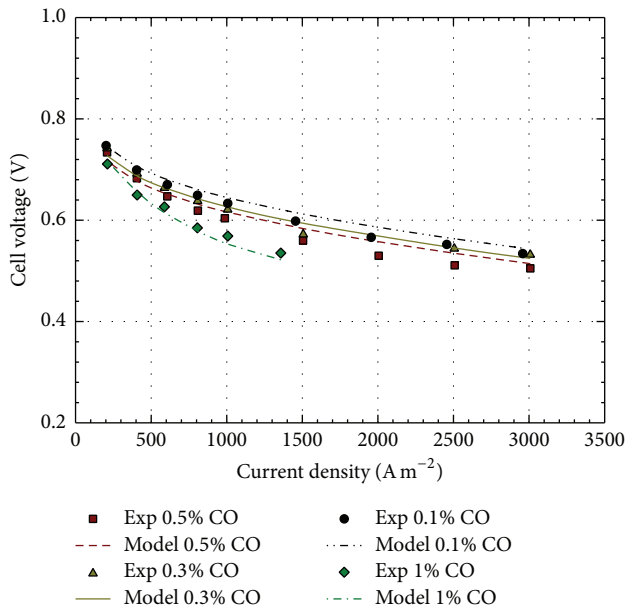

Figure 3: Validation of the voltage characteristics of the HT-PEM fuel cell stack.

Figure 4 compares the simulation, experimental, and numerical results of the dry gas composition at the outlet of the WGS reactor. The simulation results from this work agree well with these data sets. Similar to the fuel processor validation, the cogeneration system developed in this paper is validated using numerical and experimental data from literature of HT-PEM [19] and LT-PEM [25] based systems. In Zuliani and Taccani [19] commercial software Aspen Plus™ is employed to simulate the performance of a natural gas-fuelled system using energy balances. It can be noted in Table 2 that the cogeneration system in this paper compares well with the data of the HT-PEM system, showing similar

Table 2: Validation of cogeneration system.

Variable	HTPEM[a]	HTPEM[b] [19]	LTPEM[c] [25]
Operating conditions			
Current density (A/m^2)	3000	4200	2000
Operating temperature (K)	423	433	347
Steam-carbon-ratio	3	3.5	—
Fuel stoichiometry	1.25	1.2	1
Air stoichiometry	2	2	—
System outputs			
Power (W)	1000	1000	4800
Cell voltage (V)	0.55	0.5	0.74
Fuel processor efficiency (LHV)	80.9	78	—
Electrical efficiency (LHV)	27.7	26	44*
Thermal efficiency (LHV)	51.7	52	36*
Cogeneration efficiency (LHV)	79.4	78	80*
Fuel type	NG	NG	Hydrogen

*Values based on HHV
[a]Numerical data by authors
[b]Numerical data of a HT-PEM system
[c]Experimental data of a LT-PEM system.

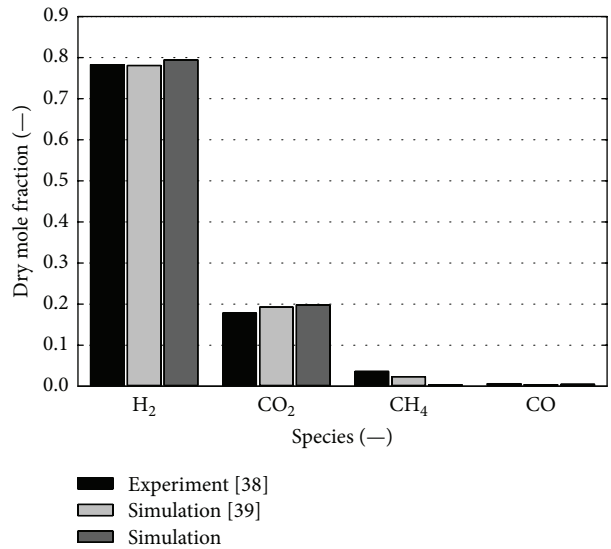

Figure 4: Comparison of the experimental and numerical dry reformate gas from the fuel processor.

electrical, fuel processor, thermal and cogeneration efficiencies. Briguglio et al. [25] conducted experiments to explore using direct water injection in the cathode of LT-PEM system operating at 73°C as a heat recovery strategy from the stack and it suitability for cogeneration application. The LT-PEM system has higher electrical efficiency of 44% (HHV) and lower thermal efficiency of 36% (HHV) when compared to the system developed by the authors.

4. Simulation Results

A parametric study was conducted to investigate the effect of different operating parameters on the system performance. Accordingly, to study the behavior of the fuel processor, the mixed effect of variation of combustor equivalence ratio

Table 3: Parameters kept constant during the simulation.

Parameter	Value
Stack operation temperature (K)	423
Current density (A/m^2)	3000
No of cells in a stack	65
Fuel cell active area (m^2)	0.01

Table 4: Operating conditions of the chosen cases.

Parameters	Case A	Case B	Case C	Case D
Equivalence ratio	0.55	0.53	0.51	0.50
Fuel ratio	0.80	0.85	0.90	0.95
Fuel processor efficiency	0.854	0.853	0.854	0.855
CO anode inlet (%)	0.34	0.42	0.57	0.72

and the fuel ratio on the performance of the systems was considered first. Based on this, a case study in which four operating points based on the combination of the two parameters was chosen.

In the four points chosen, the required constraints such as the CO concentration in the fuel cell anode inlet were met. From a design perspective, to maintain realistic dimensions of the cogeneration system, the fuel cell stack design parameters as shown in Table 3 and all heat exchangers geometries were kept constant in each of the cases considered.

4.1. Combustor Operating Parameters. As an initial investigation, the effect of variation of the combustion parameters (fuel ratio and equivalence ratio) on the fuel processor performance was investigated. The combustion of the fuel and air is a chemical reaction that strongly depends on the composition of the fuel and air fed to the combustor. The fuel ratio (FR) was defined as the ratio of the combined flow rate of combustion fuel (auxiliary CH_4 and combustible gases in the anode off-gas) to that of the CH_4 flow rate into the reformer; it was varied by increasing the auxiliary CH_4 flow rate into the combustor. The equivalence ratio (φ) was defined as the actual fuel/oxidant (air) ratio normalized by the stoichiometric fuel/oxidant ratio into the combustor [40]:

$$\varphi = \frac{(F/A)_{\text{actual}}}{(F/A)_{\text{stoich}}}. \tag{34}$$

Figure 5 presents the contour plots of the simulated cases carried out for fuel ratios range (0.75–0.95) and equivalence ratios range (0.45–0.75). The results of combined effect of the fuel ratio and equivalence ratio are summarized by plots of the temperature of the MSR and WGS reactors, fuel processor efficiency, and fuel consumption rate. Figures 5(a) and 5(b) show the temperature at the outlet of the MSR and WGS reactors. It can be seen that increasing the equivalence ratio and fuel ratio results in a rise of reactor outlet temperatures. The simulation shows that the temperatures of the reactor outlets are the highest when the φ approaches unity for all fuel ratios considered. This is caused by the increase in the heat of combustion due to increased fuel conversion in the combustor which raises the heat transferred to the reforming reactor. Figure 5(c) shows that for equivalence ratio less 0.56 the fuel processor efficiency increases with increased fuel ratios (a similar trend to the reactor temperatures). However, a peak of the efficiency is visible at different fuel ratios for equivalence ratios greater than 0.56. If the fuel ratio is higher than the peak fuel ratio the fuel processor efficiency decreases. This implies that when the reforming temperature rises above 1020 K, the fuel processor efficiency drops.

The fuel processor efficiency depends on the H_2 production rates from both the fuel MSR and WGS reactors. Increased steam reforming temperature increases the rates of the MSR reaction and decreases the WGS reaction. Because the magnitude of the reaction rate of the WGS reaction is lower on the MSR reactor, H_2 production is expected to be high in the MSR reactor at high temperatures. In the WGS reactor the effects of the high temperature operation on the WGS reaction are visible because of the magnitude of this reaction. The higher temperature results in less CO being converted to H_2, reducing the H_2 production rate from the fuel processor, which explains the peak observed in the fuel processor efficiency. Another important variable to measure the performance of the fuel processor is the fuel consumption/conversion. Figure 5(d) shows the relationship between the fuel consumption and the two fuel processor parameters. Because the fuel consumption and the fuel processor efficiency are related, they are expected to exhibit the same trend. However, the results show that the fuel consumption does not reach a peak like the fuel processor efficiency. Unlike the fuel processor efficiency, the fuel consumption only depends only on the CH_4 reforming in the MSR reactor. As mentioned above increasing the reforming temperature results in an increase in CH_4 conversion towards H_2 and CO. This explains the similar trend of the fuel consumption and the MSR reactor temperature when the fuel and equivalence ratios are varied.

It is important to consider how the fuel processor parameters affect the quality of the reformate gas produced. Lee et al. [40] showed that to maximize the synthesis gas production from a steam reformer, for use in a SOFC and MCFC, the fuel ratio should not exceed 80%. In this work the effect of varying the fuel ratio and equivalence ratio on the reformate gas composition is considered. Figure 6 presents the concentration (in dry basis) of the reformate species entering the fuel cell stack. It can be noted in Figure 6(a) that the CH_4 concentration decreases with increased equivalence ratio for range of fuel ratios. This is consistent with what is shown in Figure 5(d), illustrating the increased temperature effects on CH_4 consumption. Figure 6(c) depicts an increasing trend in the H_2 concentration when the fuel ratio is increased at every equivalence ratio. The highest value for H_2 concentration of 79.3% is obtained at high fuel and equivalence ratios. Figure 6(d) shows the carbon monoxide concentration in the fuel processor. For fuel ratios between 0.75 and 0.85, a decrease in the CO concentration is observed when the equivalence ratio is increased. However, when the equivalence ratio reaches 0.56, the CO concentration starts to increase. For fuel ratios above 0.85, the CO concentration has been observed to increase monotonically with the equivalence ratio.

4.2. System Operating Parameters. To investigate the behavior of the system at various operating conditions, four operating points, based on different combinations of fuel ratio and equivalence ratio, were chosen and are presented in Table 4.

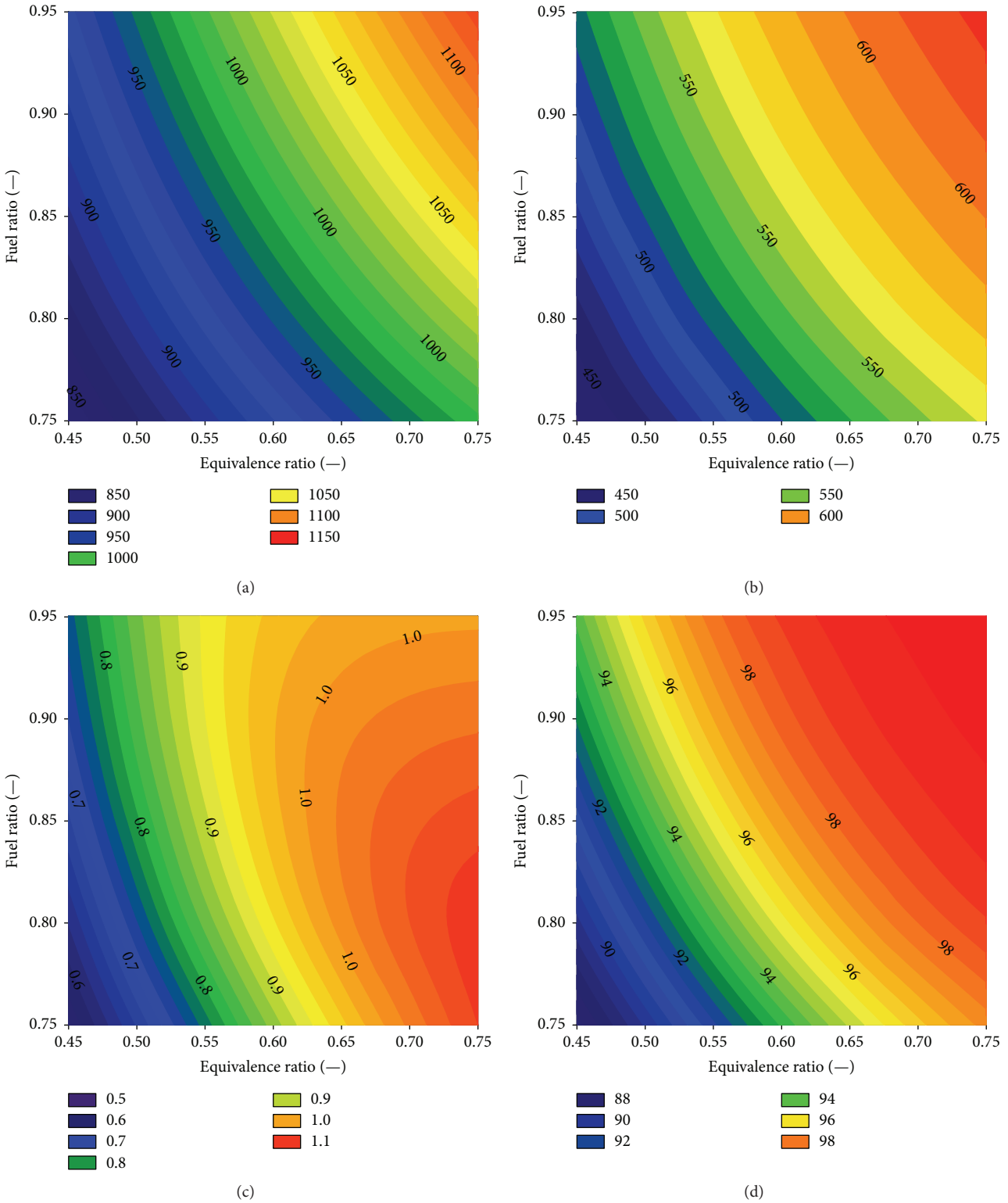

FIGURE 5: Effects of combination of fuel ratio and equivalence ratio. (a) Contours of MSR outlet temperature for varied equivalence ratio and fuel ratio. (b) Contours of WGS outlet temperature for varied equivalence ratio and fuel ratio. (c) Contour of fuel processor efficiency for varied equivalence ratio and fuel ratio. (d) Contour of fuel consumption for varied equivalence ratio.

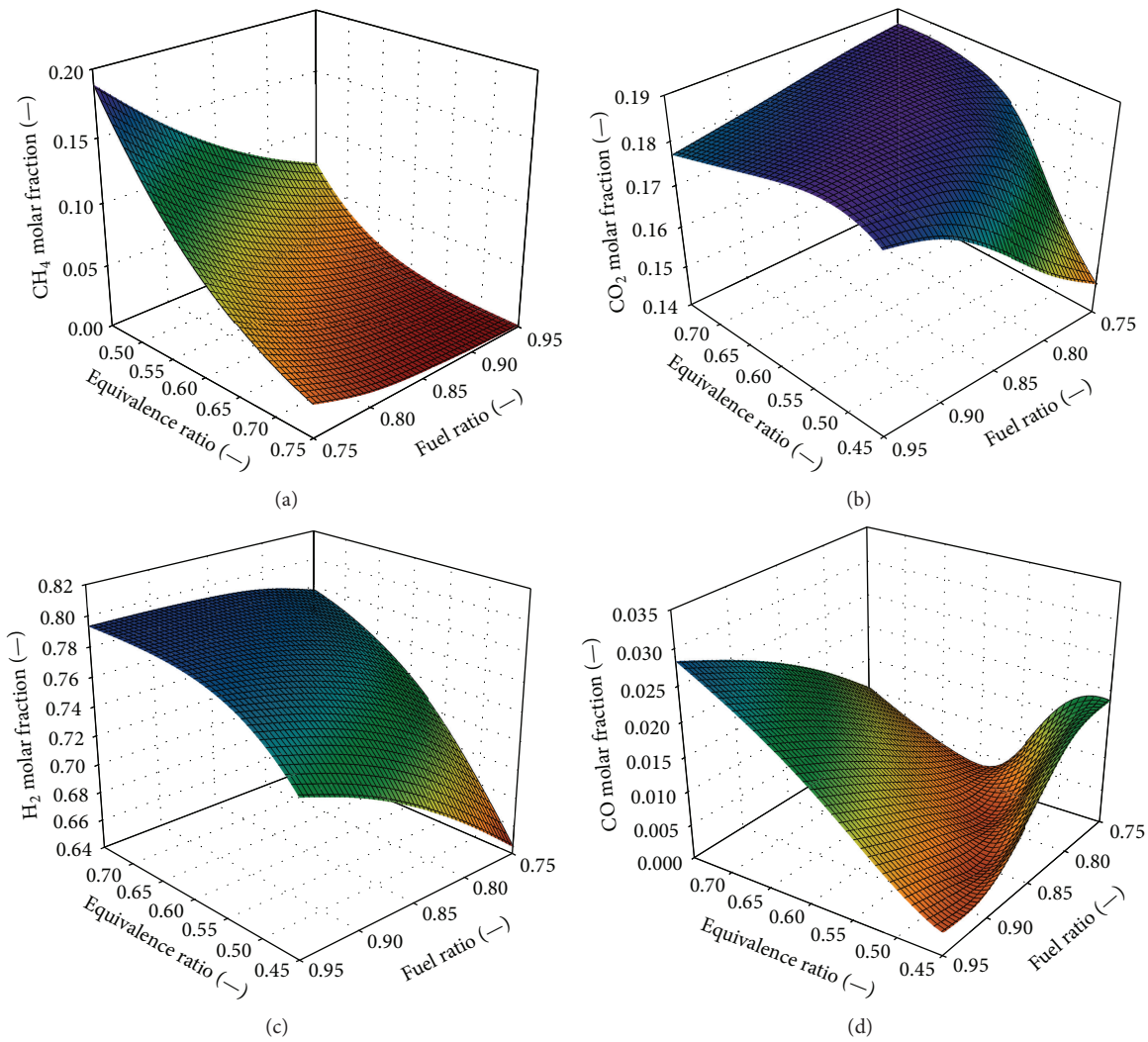

FIGURE 6: Results for reformate gas composition (dry basis) from the fuel processor with respect to equivalence and fuel ratio. (a) Methane, (b) carbon dioxide, (c) hydrogen, and (d) carbon monoxide.

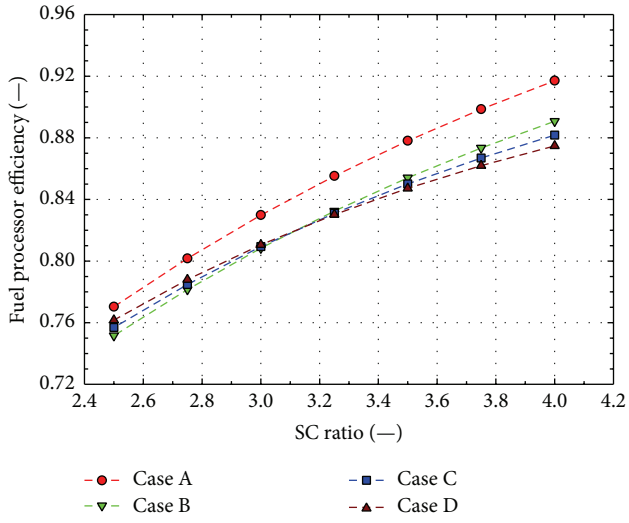

FIGURE 7: Results of fuel processor efficiency with respect to S/C ratio.

The operating points were chosen so that they cover a wide range of CO inlet into fuel cell stack. The effects of the varying the S/C ratio (2.5–4) on the performance of the fuel processor are presented in Figures 7 and 8. It can be seen in Figure 7 that increasing the S/C ratio from 2.5 to 4 results in 14.67%, 13.92%, 12.49%, and 11.3% increase in the fuel processor efficiency for cases A, B, C, and D, respectively. The main reason for this behavior is that increasing the S/C ratio has a positive effect on the kinetics of the reactors in the fuel processor. It increases the rate of the steam reforming and water-gas-shift reactions in the MSR ((1) and (2)) and the water-gas-shift reaction [20] in the shift reactor (6). The net effect of this is increased H_2 concentration (in dry basis) for the four cases in the reformate gas entering the fuel cell stack. The calculated carbon monoxide concentration (in dry basis) in the reformate gas entering the fuel cell stack for varying S/C ratio is presented in Figure 8. As it would be expected, increasing the S/C ratio from 2.5 to 4 reduces the carbon monoxide concentration by 50.5%, 57.3%, 65.6%, and

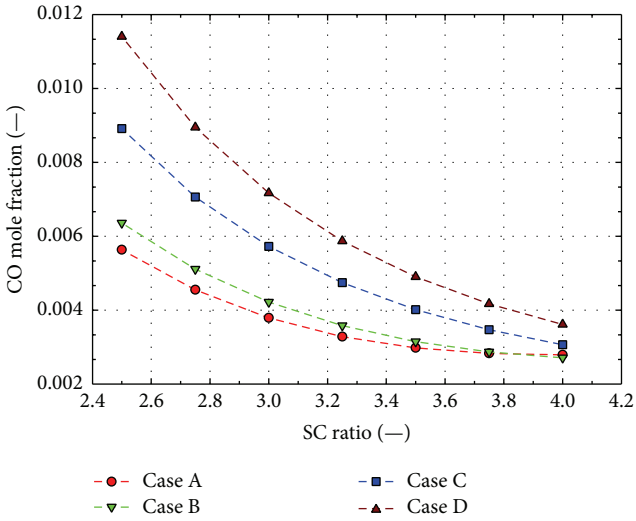

Figure 8: Results of carbon monoxide composition with respect to S/C ratio.

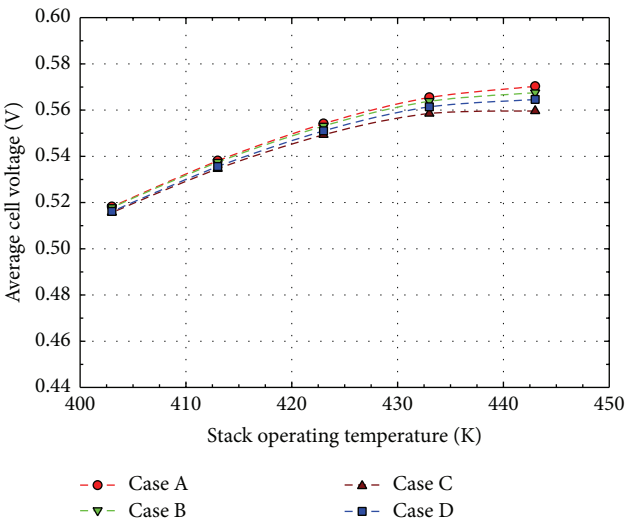

Figure 9: Results of temperature on the average stack voltage.

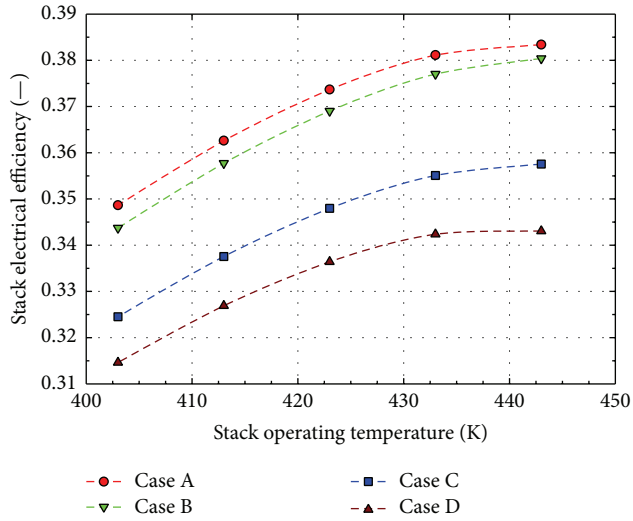

Figure 10: Results of temperature on the stack electrical efficiency.

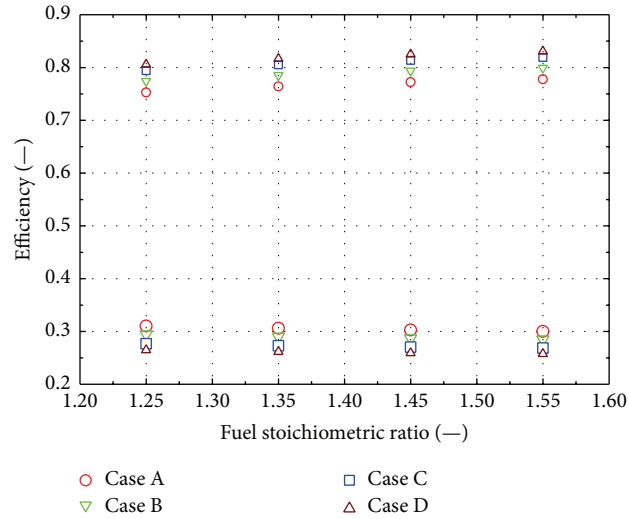

Figure 11: Results of electrical and cogeneration efficiency with respect to anode stoichiometry.

68.3% for cases A, B, C, and D, respectively. The decrease in CO concentration and strong influence in fuel processor efficiency is in agreement with work published by Ersöz and Sayar [41] for an Autothermal Reforming based system.

The effect of varying the fuel cell stack operating temperature in the performance of the system is shown in Figures 9 and 10. From Figure 9, it is observed that increasing the stack operating temperature results in an increase in the stack average cell voltage for all cases considered as expected. This is a result of improved reaction kinetics in the cell catalyst layer that decreases the associated cell voltage losses [32]. To explain the observed behavior for each case in Figure 9, we consider two cases (A and D). The operating points for each case in Table 4 lead to different carbon monoxide composition in the stack anode inlet, lowest in case A (0.32%) and highest in case D (0.72%). As a result of this, case A results in the highest cell voltage and case D in the lowest one for all temperatures. It can be also noted that while there is small difference in the cell voltage at lower temperatures, case A and case B show better performance at high temperatures because of the low CO content in the anode inlet. Figure 10 presents the variation of the stack electrical efficiency at different stack operating temperatures. Because the power generated in the stack is proportional to the stack voltage, a trend similar to that of the voltage at different operating temperature is observed [20].

The anode stoichiometric ratio is an important parameter in the system as it determines the concentration of fuel in the combustor [42] and operating temperature. Simulations of system performance were conducted at four anode stoichiometric ratios (1.25–1.55) and the results are presented in Figure 11. As the stoichiometric ratio is increased, the molar fraction of hydrogen in the anode off-gas is increased. This results in increased temperature in the combustor and reformer, thus increasing the fuel processor efficiency and

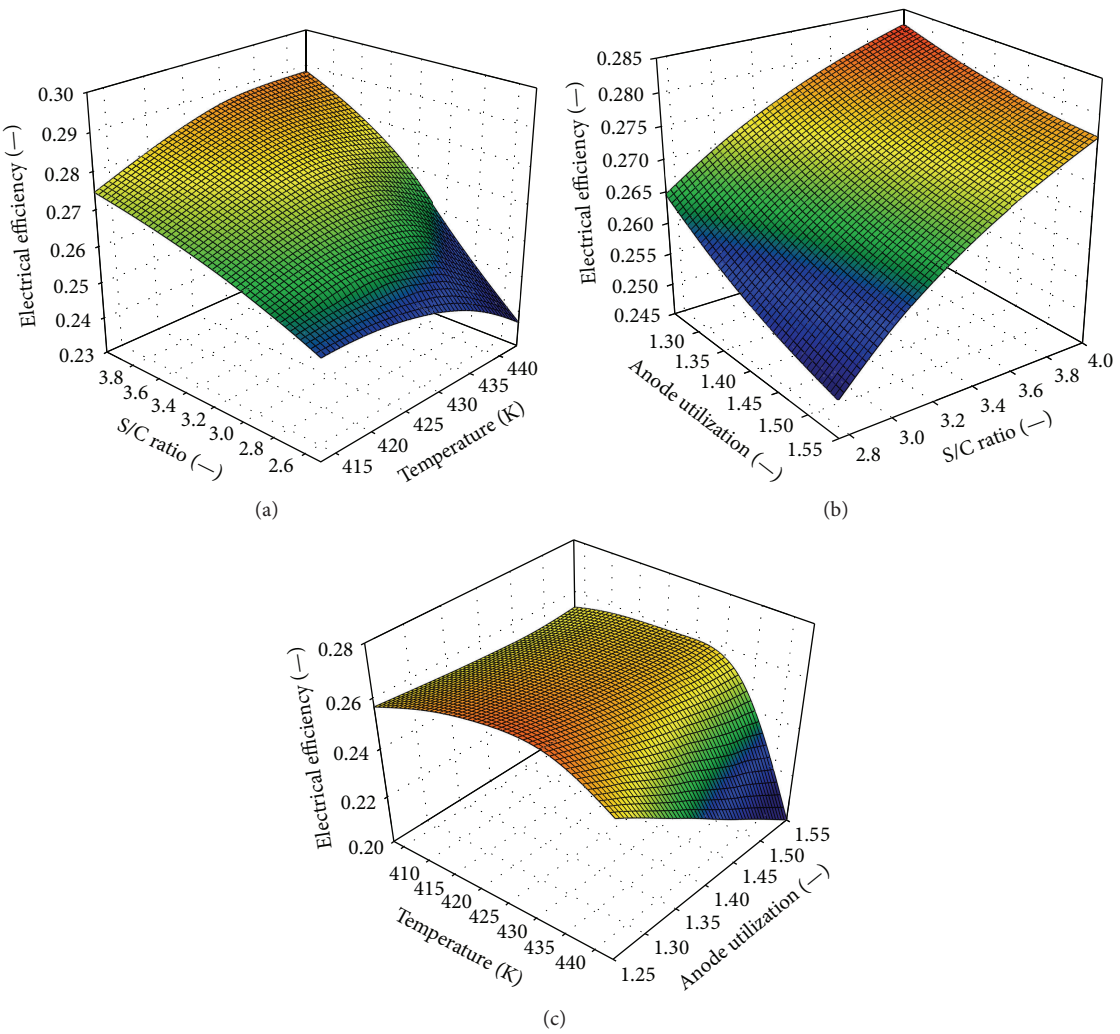

Figure 12: Sensitivity of the electrical efficiency with respect to (a) temperature and S/C ratio, (b) anode utilization and S/C ratio, and (c) temperature and anode utilization.

system thermal efficiency. Increased temperature of combustion gases also leads to large amounts of heat available for thermal power generation in cogeneration heat exchanger (HX-1). An increasing trend was observed in the cogeneration efficiency from 79% to 82% as a result of an increment (from 1.25 to 1.55) in the anode stoichiometric ratio for case C. Although increasing the stoichiometric ratio results in better cogeneration efficiency, this is to the detriment of the stack electrical efficiency as it decreases. The higher heat transferred to the reformer leads to increased CO levels in the anode inlet, which subsequently results in decreased cell voltage. The effect of the stoichiometric ratio on the electrical efficiency is also shown in Figure 11 and a decreasing trend can be observed for all the cases considered.

Surface plots were generated in order to investigate the sensitivity of the electrical and cogeneration efficiency to the changes in the three parameters. In doing so, the effect of changing two parameters within one simulation can be determined. For this analysis case C has been considered. Figures 12 and 13 present the sensitivity of the electrical and cogeneration efficiencies of the system. The system optimal point for maximum electrical efficiency can be defined from Figures 12(a), 12(b), and 12(c). It corresponds to high S/C ratio, high temperature, and lower anode stoichiometry. In a similar manner, surface plots depicting the sensitivity of the cogeneration efficiency to the three parameters are presented in Figures 13(a), 13(b), and 13(c). For maximizing cogeneration efficiency high anode stoichiometry, high S/C ratio, and high temperature present the optimal point. The selection of maximizing electrical or cogeneration efficiency depends on the operation strategy selected by the end user [43]. The two commonly used strategies are the electrical load driven and thermal load driven operations. For electricity load driven operation where the system is operated to meet the electrical demand, operating point which maximizes the electrical efficiency would be considered as optimal. Similarly for a user with high thermal load demand, maximizing the cogeneration efficiency would be preferred.

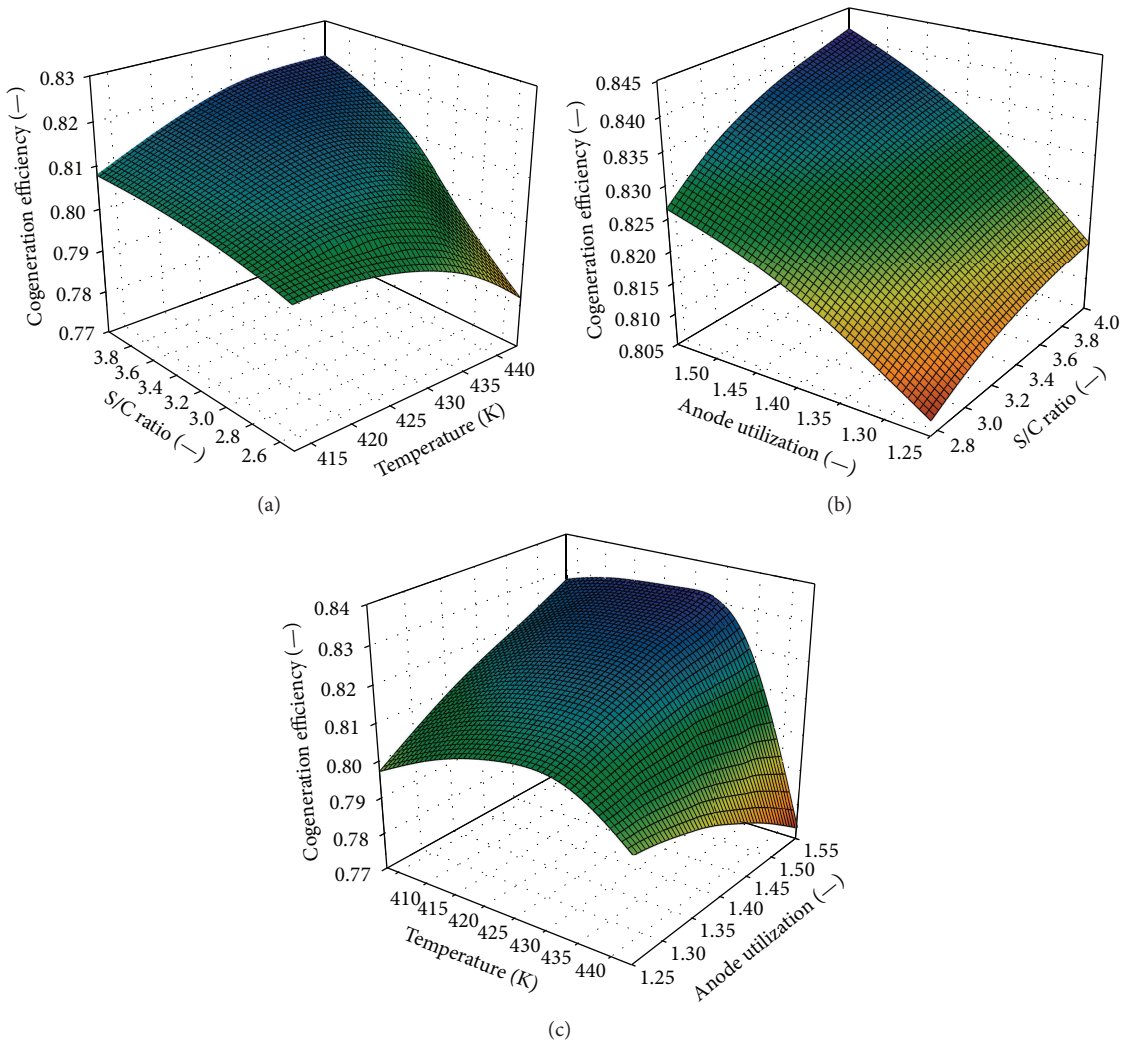

FIGURE 13: Sensitivity of the cogeneration efficiency with respect to (a) temperature and S/C ratio, (b) anode utilization and S/C ratio, and (c) temperature and anode utilization.

5. Conclusions

In this work, a model for a 1 kW_e HT-PEM fuel cell cogeneration system suitable for residential application is presented. In the first part of our investigations, a parametric study of the combustor parameters (fuel ratio and equivalence ratio) was conducted. It is shown that while higher fuel ratio and equivalence ratio lead to high fuel processor efficiencies, they result in high levels of CO content in the reformate gas that are not acceptable to the fuel cell stack. Using four operating points that represent the combination of fuel ratio and equivalence ratio, a parametric study of the cogeneration system was conducted. Variation of the steam-carbon ratio, stack operating temperature, and anode stoichiometric ratio on the system performance was considered. Increasing the SC ratio (2.5–4.0) resulted in increased fuel processor performance, reducing the anodic CO molar fraction to less than 0.4% for all the cases. The stack average cell voltage was shown to increase as a result of lower CO molar fraction in the anode inlet. It was shown that increasing the stack operating temperature (403–443 K) increased the electrical efficiency from 34.84% to 38.34% for case A. It was also shown that while high temperature operation results in increased voltage for all cases, better performance for cases with lower CO content is obtained at high temperatures. Increasing the anode stoichiometric ratio from 1.25 to 1.55 has a positive impact on the cogeneration efficiency while the electrical efficiency dropped, showing that the anode stoichiometry can be useful in regulating the system load demands.

Symbols

c: Concentration (mol/m^3)
Cr: Heat capacity ratio
E_a: Activation energy (kJ/mol)
F: Faraday constant (C/mol)
HEX: Heat exchanger
j: Exchange current density (A/m)
k: Reaction rate constant (kmol $bar^{0.5}/kg_{cat}$ h)
K: Adsorption constant (1/bar)

K_{eq}: Equilibrium constant
LHV: Lower heating value (kJ/kg)
$\dot{m}$: Mass flow rate (kg/s)
n: Number of electrons transferred
NTU: Number of transfer units
p: Partial pressure (Pa)
r: Reaction rate (kmol/s kg_{cat})
R: Universal gas constant (kJ/kmol K)
T: Temperature (K)
U: Voltage (V)
P: Power (W)
W: Acid doping level (—)
y: Mole fraction (—).

Greek

η: Efficiency
ε: Heat exchanger effectiveness
α: Transfer coefficient
θ_{CO}: Fraction of catalyst surface covered by CO.

Subscripts and Superscripts

act: Activation
a: Anode
c: Cathode
cell: Single cell
cogen: Cogeneration
el: Electrical
eq: Equilibrium
i: Component
j: Reaction
ocv: Open-circuit voltage
ohm: Ohmic
ox: Oxidation
rd: Reduction
th: Thermal.

Competing Interests

The authors declare that there is no conflict of interests regarding the publication of this paper.

Acknowledgments

The financial assistance of the National Research Foundation (NRF) towards this research is hereby acknowledged. Opinions expressed and conclusions arrived at are those of the authors and are not necessarily to be attributed to the NRF. The authors would like to thank Dr. Yusuf Isa from the Durban University of Technology for his assistance in the development of the models.

References

[1] G. Angrisani, C. Roselli, and M. Sasso, "Distributed microtrigeneration systems," *Progress in Energy and Combustion Science*, vol. 38, no. 4, pp. 502–521, 2012.

[2] D. Sonar, S. L. Soni, and D. Sharma, "Micro-trigeneration for energy sustainability: technologies, tools and trends," *Applied Thermal Engineering*, vol. 71, no. 2, pp. 790–796, 2014.

[3] J. Geraldo de Melo Furtado, G. C. Gatti, E. T. Serra, and S. C. Anibal De Almeida, "Performance analysis of a 5 kW PEMFC with a natural gas reformer," *International Journal of Hydrogen Energy*, vol. 35, no. 18, pp. 9990–9995, 2010.

[4] FuelCellToday, *The Fuel Cell Industry Review*, 2013.

[5] L. Xiao, H. Zhang, T. Jana et al., "Synthesis and characterization of pyridine-based polybenzimidazoles for high temperature polymer electrolyte membrane fuel cell applications," *Fuel Cells*, vol. 5, no. 2, pp. 287–295, 2005.

[6] J. Zhang, J. Wu, H. Zhang, and J. Zhang, "High-temperature PEM fuel cells," in *Pem Fuel Cell Testing and Diagnosis*, J. Zhang, J. Wu, H. Zhang, and J. Zhang, Eds., chapter 10, pp. 243–282, Elsevier, Amsterdam, The Netherlands, 2013.

[7] Z. Qi and S. Buelte, "Effect of open circuit voltage on performance and degradation of high temperature PBI-H_3PO_4 fuel cells," *Journal of Power Sources*, vol. 161, no. 2, pp. 1126–1132, 2006.

[8] L. Qingfeng, H. A. Hjuler, and N. J. Bjerrum, "Phosphoric acid doped polybenzimidazole membranes: physiochemical characterization and fuel cell applications," *Journal of Applied Electrochemistry*, vol. 31, no. 7, pp. 773–779, 2001.

[9] N. H. Jalani, M. Ramani, K. Ohlsson et al., "Performance analysis and impedance spectral signatures of high temperature PBI-phosphoric acid gel membrane fuel cells," *Journal of Power Sources*, vol. 160, no. 2, pp. 1096–1103, 2006.

[10] Q. Li, R. He, J.-A. Gao, J. O. Jensen, and N. J. Bjerrum, "The CO poisoning effect in PEMFCs operational at temperatures up to 200°C," *Journal of the Electrochemical Society*, vol. 150, no. 12, pp. A1599–A1605, 2003.

[11] U. Gardemann, M. Steffen, and A. Heinzel, "Design and demonstration of an ethanol fuel processor for HT-PEM fuel cell applications," *International Journal of Hydrogen Energy*, vol. 39, no. 31, pp. 18135–18145, 2014.

[12] M. Maximini, P. Engelhardt, M. Brenner, F. Beckmann, and O. Moritz, "Fast start-up of a diesel fuel processor for PEM fuel cells," *International Journal of Hydrogen Energy*, vol. 39, no. 31, pp. 18154–18163, 2014.

[13] R. C. Samsun, C. Krupp, A. Tschauder, R. Peters, and D. Stolten, "Electrical start-up for diesel fuel processing in a fuel-cell-based auxiliary power unit," *Journal of Power Sources*, vol. 302, pp. 315–323, 2016.

[14] S. Authayanun, W. Wiyaratn, S. Assabumrungrat, and A. Arpornwichanop, "Theoretical analysis of a glycerol reforming and high-temperature PEMFC integrated system: hydrogen production and system efficiency," *Fuel*, vol. 105, pp. 345–352, 2013.

[15] A. Perna, S. P. Cicconardi, and R. Cozzolino, "Performance evaluation of a fuel processing system based on membrane reactors technology integrated with a PEMFC stack," *International Journal of Hydrogen Energy*, vol. 36, no. 16, pp. 9906–9915, 2011.

[16] S. Authayanun, M. Mamlouk, K. Scott, and A. Arpornwichanop, "Comparison of high-temperature and low-temperature polymer electrolyte membrane fuel cell systems with glycerol reforming process for stationary applications," *Applied Energy*, vol. 109, pp. 192–201, 2013.

[17] E. Jannelli, M. Minutillo, and A. Perna, "Analyzing microcogeneration systems based on LT-PEMFC and HT-PEMFC by energy balances," *Applied Energy*, vol. 108, pp. 82–91, 2013.

[18] A. Arsalis, M. P. Nielsen, and S. K. Kær, "Modeling and off-design performance of a 1kWe HT-PEMFC (high temperature-proton exchange membrane fuel cell)-based residential micro-CHP (combined-heat-and-power) system for Danish single-family households," *Energy*, vol. 36, no. 2, pp. 993–1002, 2011.

[19] N. Zuliani and R. Taccani, "Microcogeneration system based on HTPEM fuel cell fueled with natural gas: performance analysis," *Applied Energy*, vol. 97, pp. 802–808, 2012.

[20] B. Najafi, A. Haghighat Mamaghani, A. Baricci, F. Rinaldi, and A. Casalegno, "Mathematical modelling and parametric study on a 30 kWel high temperature PEM fuel cell based residential micro cogeneration plant," *International Journal of Hydrogen Energy*, vol. 40, no. 3, pp. 1569–1583, 2015.

[21] A. M. Rabiu, N. Dlangamandla, and Ø. Ulleberg, "Novel heat integration in a methane reformer and high temperature PEM fuel cell-based mCHP system," *APCBEE Procedia*, vol. 3, pp. 17–22, 2012.

[22] A. Arsalis, M. P. Nielsen, and S. K. Kær, "Optimization of a high temperature PEMFC micro-CHP system by formulation and application of a process integration methodology," *Fuel Cells*, vol. 13, no. 2, pp. 238–248, 2013.

[23] A. Arsalis, S. K. Kær, and M. P. Nielsen, "Modeling and optimization of a heat-pump-assisted high temperature proton exchange membrane fuel cell micro-combined-heat-and-power system for residential applications," *Applied Energy*, vol. 147, pp. 569–581, 2015.

[24] B. Najafi, A. Haghighat Mamaghani, F. Rinaldi, and A. Casalegno, "Long-term performance analysis of an HT-PEM fuel cell based micro-CHP system: operational strategies," *Applied Energy*, vol. 147, pp. 582–592, 2015.

[25] N. Briguglio, M. Ferraro, G. Brunaccini, and V. Antonucci, "Evaluation of a low temperature fuel cell system for residential CHP," *International Journal of Hydrogen Energy*, vol. 36, no. 13, pp. 8023–8029, 2011.

[26] J. Xu and G. F. Froment, "Methane steam reforming, methanation and water-gas shift: I. Intrinsic kinetics," *AIChE Journal*, vol. 35, no. 1, pp. 88–96, 1989.

[27] G.-Y. Kim, J. R. Mayor, and J. Ni, "Parametric study of microreactor design for water gas shift reactor using an integrated reaction and heat exchange model," *Chemical Engineering Journal*, vol. 110, no. 1–3, pp. 1–10, 2005.

[28] R. W. Schefer, "Catalyzed combustion of H2/air mixtures in a flat plate boundary layer: II. Numerical model," *Combustion and Flame*, vol. 45, pp. 171–190, 1982.

[29] X. Song, W. R. Williams, L. D. Schmidt, and R. Aris, "Ignition and extinction of homogeneous-heterogeneous combustion: CH_4 and C_3H_8 oxidation on PT," *Symposium (International) on Combustion*, vol. 23, no. 1, pp. 1129–1137, 1991.

[30] N. W. Cant, P. C. Hicks, and B. S. Lennon, "Steady-state oxidation of carbon monoxide over supported noble metals with particular reference to platinum," *Journal of Catalysis*, vol. 54, no. 3, pp. 372–383, 1978.

[31] K. Jiao, I. E. Alaefour, and X. Li, "Three-dimensional non-isothermal modeling of carbon monoxide poisoning in high temperature proton exchange membrane fuel cells with phosphoric acid doped polybenzimidazole membranes," *Fuel*, vol. 90, no. 2, pp. 568–582, 2011.

[32] K. Scott and M. Mamlouk, "A cell voltage equation for an intermediate temperature proton exchange membrane fuel cell," *International Journal of Hydrogen Energy*, vol. 34, no. 22, pp. 9195–9202, 2009.

[33] D. F. Cheddie and N. D. H. Munroe, "A two-phase model of an intermediate temperature PEM fuel cell," *International Journal of Hydrogen Energy*, vol. 32, no. 7, pp. 832–841, 2007.

[34] T. Sousa, M. Mamlouk, and K. Scott, "An isothermal model of a laboratory intermediate temperature fuel cell using PBI doped phosphoric acid membranes," *Chemical Engineering Science*, vol. 65, no. 8, pp. 2513–2530, 2010.

[35] H. P. Dhar, L. G. Christner, A. K. Kush, and H. C. Maru, "Performance study of a fuel cell Pt-on-C anode in presence of CO and CO_2 and calculation of adsorption parameters for CO poisoning," *Journal of the Electrochemical Society*, vol. 133, no. 8, pp. 1574–1582, 1986.

[36] PSE, "*gPROMS ModelBuilder v3.6*," 2015, http://www.psenterprise.com/.

[37] P. Bujlo, S. Pasupathi, Ø. Ulleberg et al., "Validation of an externally oil-cooled 1 kWel HT-PEMFC stack operating at various experimental conditions," *International Journal of Hydrogen Energy*, vol. 38, no. 23, pp. 9847–9855, 2013.

[38] D. Di Bona, E. Jannelli, M. Minutillo, and A. Perna, "Investigations on the behaviour of 2 kW natural gas fuel processor," *International Journal of Hydrogen Energy*, vol. 36, no. 13, pp. 7763–7770, 2011.

[39] U. H. Jung, W. Kim, K. Y. Koo, and W. L. Yoon, "Genuine design of compact natural gas fuel processor for 1-kWe class residential proton exchange membrane fuel cell systems," *Fuel Processing Technology*, vol. 121, pp. 32–37, 2014.

[40] C.-B. Lee, S.-H. Cho, D.-W. Lee, K.-R. Hwang, J.-S. Park, and S.-H. Kim, "Combination of preferential CO oxidation and methanation in hybrid MCR (micro-channel reactor) for CO clean-up," *Energy*, vol. 78, pp. 421–425, 2014.

[41] A. Ersöz and A. Sayar, "A process simulation study of a newly designed fuel processing system for a high temperature PEM fuel cell unit," *International Journal of Hydrogen Energy*, vol. 40, no. 42, pp. 14469–14482, 2015.

[42] A. Arsalis, M. P. Nielsen, and S. K. Kær, "Modeling and parametric study of a 1 kWe HT-PEMFC-based residential micro-CHP system," *International Journal of Hydrogen Energy*, vol. 36, no. 8, pp. 5010–5020, 2011.

[43] J. Kupecki, "Off-design analysis of a micro-CHP unit with solid oxide fuel cells fed by DME," *International Journal of Hydrogen Energy*, vol. 40, no. 35, pp. 12009–12022, 2015.